Mechanisms of Particle Dispersion in a Turbulent, Square Duct Flow

Michael Fairweather and Jun Yao
Institute of Particle Science and Engineering, School of Process, Environmental and Materials Engineering, University of Leeds, Leeds LS2 9JT, U.K

DOI 10.1002/aic.11798
Published online June 8, 2009 in Wiley InterScience (www.interscience.wiley.com).

Particle dispersion in a square duct flow is studied using large eddy simulation combined with Lagrangian particle tracking under conditions of one-way coupling. The flow has a bulk Re = *250 k, with six particle sizes ranging from 5 to 1000 μm. Results obtained for the fluid phase show good agreement with experimental data. For particles, predictions demonstrate that secondary flows within the duct dominate small particle dispersion and result in a uniform distribution, whereas gravity promotes the deposition of large particles on the duct floor. For the largest particles, the secondary flows contribute to particle concentration in corners on the duct floor, with these particles also clustering in low-velocity regions close to the floor. A detailed analysis of the influence of the flow on particle distribution is provided through consideration of the particle dispersion function, with the mechanisms of particle dispersion elucidated using a dynamical analysis.* © 2009 American Institute of Chemical Engineers *AIChE J,* 55: 1667–1679, 2009

Keywords: large eddy simulation, secondary flow, particle, dispersion, square duct

Introduction

Understanding the mechanisms of particle dispersion in turbulent flows is important in many industrial, environmental, and energy-related processes. For example, in the management of dust in clean rooms, chemical reactions involving a particulate catalyst, the flow of liquid and gas mixtures through process equipment, and in the combustion of liquid sprays. Of particular interest is the processing and transportation of nuclear waste, which is stored as a liquid–solid sludge, and its behavior in terms of the settling or nonsettling characteristics of particles, their propensity to form solid beds, and the resuspension characteristics of particles from a bed. The formation of particle beds can result in blockages to pipes and equipment and lead to difficulties in obtaining dispersed particle flows from storage equipment for subsequent processing. The pumping of waste along pipes or ducts also gives rise to highly complex flows, where secondary flows caused, for example, by pipe bends can induce particle deposition. An understanding of how these flows behave during transportation is of clear benefit to more cost-effective process design, continued operation, and accelerated waste clean-up.

A great deal of work has been carried out to understand the mechanisms of particle dispersion in a variety of flows, for example, the plane wake, mixing layers, jet flows, and flows around a bluff body. Tang et al.[1] used experimental and numerical methods to study the particle dispersion mechanisms in a plane wake and demonstrated the importance of large-scale vortex structures in self-organizing dispersion processes. Ling et al.[2] and Fan et al.[3] used direct numerical simulation to examine the dispersion of particles in three-dimensional mixing layers, which are dominated by large-scale, two-dimensional turbulent structures. Yuu et al.[4] investigated the turbulent diffusion mechanism of particles in a round jet and concluded that particle inertia and large-scale turbulent eddies play an important role in the transport of particles. More recently, these findings were confirmed by Fairweather and Hurn[5] who developed an anisotropic model of turbulent flows containing dispersed solid particles which was applied to gas–solid jets. Morsi and Alexander[6]

Correspondence concerning this article should be addressed to J. Yao at j.yao@leeds.ac.uk.

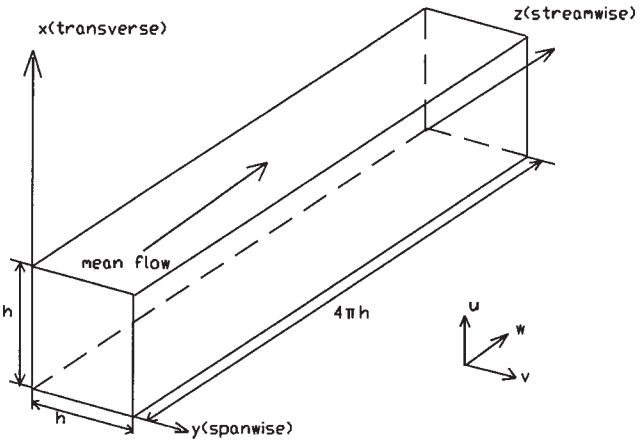

Figure 1. Schematic diagram of the duct geometry and coordinate system.

examined a two-phase flow around a cylinder and found that the effect of the lift force is small when compared with that of the drag force. Yao et al.[7] also used direct numerical simulation to study the same problem and found that the mechanism of particle dispersion in the flow mainly depends on the repulsion force associated with the vortex sheet regions between two adjacent vortex structures with opposite sign. However, for particle-laden flows in a straight duct (square or rectangular), less work has been performed, and there is limited understanding of the mechanisms of particle dispersion.

A number of studies have focused on turbulent single-phase flows through square ducts, including experimental investigations,[8–10] direct numerical simulations,[11] and large eddy simulations (LES).[12] All of these studies have demonstrated that turbulence-driven secondary motions that arise in duct flows act to transfer fluid momentum from the center of the duct to its corners, thereby causing a bulging of the streamwise velocity contours toward the corners. They also established that the Reynolds normal and shear stresses contribute equally to the production of mean streamwise vorticity. When compared with single-phase flows, there exist few studies of particle-laden turbulent flows in a duct. To date, two groups have conducted simulations in this field. Winkler et al.[13] applied LES, coupled with Langrangian particle tracking, to study the preferential concentration of heavy particles in a duct flow, with their work focusing on particles with a low response time ($St = 0.25$–8). Sharma and Phares[14] also used direct numerical simulation and Langrangian particle tracking to study the secondary flow effects on particle transport and deposition in a square duct flow. However, in the latter work, the effects of gravity were neglected despite the consideration of large, heavy particle behavior in such flows. Both groups also focused on low Reynolds number turbulent flows ($Re_\tau = 360$ and 300, respectively, based on the mean friction velocity and the duct width). As a consequence, particle dispersion mechanisms in square duct flows, particularly at high Reynolds numbers, have not been fully elucidated.

In this work, LES coupled with a Langrangian particle tracking technique was used to study the heavy particle dispersion in a high Reynolds number flow ($Re_\tau = 10{,}550$) in a straight, square duct. A wide range of particle sizes ($St = 0.24$–9661) have been investigated, with the distribution of particle velocity and position in the duct cross-section simulated, and the contribution of the secondary flow and gravity force to particle dispersion analyzed. Further, the particle dispersion function has been applied to describe dispersion in the duct flow. Particle segregation and concentration near the floor of the duct are found to depend on particle size, and the link to flow turbulence is investigated. The mechanisms of particle dispersion in a duct flow are then considered using a dynamical analysis which examines the main forces acting on a particle (gravity, buoyancy, and drag), as well as the relative slip velocity and secondary flow effects.

Mathematical Model

Flow configuration

A schematic diagram of the duct geometry and coordinate system used is shown in Figure 1. The flow is three-dimensional and described by a Cartesian coordinate system (x, y, z), in which the z axis is aligned with the streamwise flow direction, the x axis is in the direction normal to the floor of the duct, and the y axis is in the spanwise direction. The corresponding velocity components in the (x, y, z) directions are (u, v, w). In modeling this flow, the boundary conditions for the momentum equations were no-slip at the duct walls. To avoid having to specify inflow and outflow conditions at the open boundaries of the duct, it was assumed that the instantaneous flow field was periodic along the streamwise direction, with the pressure gradient that drives the flow adjusted dynamically to maintain a constant mass flux through the duct. The friction Reynolds number, $Re_\tau = hu_\tau/\upsilon$, for the simulations was 10,550, corresponding to a bulk Reynolds number $Re_b \sim 250{,}000$.

The dimensions of the square duct were $h \times h \times 4\pi h$ (see Figure 1), which in terms of wall units gives $L_x^+ = L_y^+ = 10{,}550$ and $L_z^+ = 132{,}576$. The streamwise length is sufficiently long to accommodate the streamwise-elongated, near-wall structures present in wall-bounded shear flows, with such structures rarely expected to be longer than $\sim$1000 wall units.[15] Sensitivity studies were performed using various numerical grid distributions and numbers of computational nodes, and for the final grid arrangements, selected turbulence statistics were found to be independent of grid resolution. Based on the uniform Cartesian grid employed, $66 \times 66 \times 130$, the grid resolution was $\Delta x^+ = \Delta y^+ = 159.85$ wall units in the wall-normal directions and $\Delta z^+ = 1019.82$ in the streamwise direction. A second simulation using an increased total number of nonuniformly distributed nodes was also used to give better resolution near the floor of the duct. This used a minimum grid resolution of $\Delta x^+ = \Delta y^+ = 6.39$ wall units in the wall-normal directions and $\Delta z^+ = 40.80$ in the streamwise direction, and it was performed over one-third the height of the original domain, with the upper boundary patched on to the velocity field generated by the full domain solution. To save computational effort, the coarse grid was employed for general analysis, with the near-wall simulation used to give detailed flow information near the wall boundary. The dimensionless integration time step used was $\Delta t = 6.66 \times 10^{-5}$ or, equivalently, $\Delta t^+ = 7.03 \times 10^{-1}$.

Large eddy simulation

In LES, only the large energetic scales of motion are directly computed, whereas the small scales are modeled. Any function is decomposed using a localized filter function, such that filtered values only retain the variability of the original function over length scales comparable with or larger than that of the filter width. In this work, a top hat filter was used as it fits naturally into a finite-volume formulation. This decomposition is then applied to the Navier-Stokes equations, for an incompressible Newtonian fluid with constant properties, giving rise to terms which represents the effect of the subgrid scale (SGS) motion on the resolved motion. The SGS stress model used was the dynamic model of Germano,[16] implemented using the approximate localization procedure of Piomelli and Liu[17] together with the modification proposed by di Mare and Jones.[18] This model represents the SGS stress as the product of a SGS viscosity and the resolved part of the strain tensor, and it is based on the possibility of allowing different values of the Smagorinsky constant at different filter levels. In this formulation, the model parameter is numerically well behaved, and the method is well conditioned and avoids the irregular behavior exhibited by some implementations of the dynamic model. Test filtering was performed in all space directions, with no averaging of the computed model parameter field.

Computations were performed using the computer program BOFFIN.[19] The code implements an implicit finite-volume incompressible flow solver using a colocated variable storage arrangement. Because of this arrangement, fourth-order pressure smoothing, based on the method proposed by Rhie and Chow,[20] is applied to prevent spurious oscillations in the pressure field. Time advancement is performed via an implicit Gear method for all transport terms, and the overall procedure is second-order accurate in both space and time. A constant time step was chosen by requiring that the maximum Courant number lies between 0.1 and 0.3, with this requirement enforced for reasons of accuracy.[21] The code is parallel and uses the message passing interface MPI-1.2. Time-averaged flow field variables reported later were computed from running averages during the computations.

Further details of the mathematical model employed, and the numerical algorithm and its implementation, may be found in Refs. 18 and 19.

Lagrangian particle tracking

From the fluid velocity field V, particle motion was modeled using a Lagrangian approach[22] in which the particles are followed along their trajectories through the unsteady, nonuniform flow field. To simplify the analysis, the following assumptions were made: the particle-laden flow is dilute; interactions between particles are negligible; the flow and particles are one-way coupled, i.e., the effect of particles on the fluid is neglected; all particles are rigid spheres with the same diameter and density; and particle-wall collisions are elastic. The Lagrangian motion of a rigid, spherical particle suspended in a flow is governed by a force balance equation as follows:

$$\frac{dV_p}{dt} = \frac{3}{4}\frac{\rho}{\rho_p}\frac{C_D}{d_p}(V - V_p)|V - V_p| + \left(1 - \frac{\rho}{\rho_p}\right)g, \qquad (1)$$

where V_p is the particle velocity, ρ_p is the particle density, d_p is the particle diameter, ρ is the fluid density, and g is the gravity. C_D is the Stokes coefficient for drag, with $C_D = (1 + 0.15\ Re_p^{0.687}) \times 24/Re_p$, where Re_p is the particle Reynolds number, $Re_p = d_p|V - V_p|/v$. Even though a number of possible forces can act on a particle, many of these may be neglected without any appreciable loss of accuracy, depending on the particle inertia. The most important force acting on the particle is the Stokes drag force, with gravity also important depending on the orientation of the flow. In this study, Stokes drag, gravity, and buoyancy forces were considered, although the shear-induced Saffman lift force[23] was neglected because it only assumes nontrivial magnitudes in the viscous sublayer. Even in this region, however, it has been found to be an order of magnitude smaller than the normal component of the Stokes drag force.[24] Because of the particle-wall impaction, electrostatic charge can be generated at the particle surface and the duct wall.[25] In this work, the straight square duct is set in the horizontal direction, such that the electrostatic force acting on a particle is much lower than the gravity effect by at least two orders of magnitude,[26] and consequently can be neglected. Other forces acting on the particle, such as the hydrostatic force, Magnus effect, Basset history force, and added mass force, were not taken into account due to their orders of magnitude being smaller than the three effects considered.[27]

A fourth-order Runge-Kutta scheme was used to solve the equation of motion, given the initial particle location and velocity. The initial particle positions were distributed randomly throughout the duct, corresponding to an initially uniform wall-normal particle number density profile. The initial particle velocity was set equal to the fluid velocity, interpolated to the particle position. Particles were assumed to interact with turbulent eddies over a certain period of time, that is, being lesser of the eddy lifetime and the transition time. For particles that moved out of the square duct in the streamwise direction, periodic boundary conditions were used to reintroduce them into the computational domain. The total number of particles considered in the computational domain ranged from 10,000 to 100,000 in all cases, with the precise number employed being sufficient to ensure statistical independence of the results.

Particle and flow densities were set to $\rho_p = 2500$ kg m^{-3} and $\rho = 1000$ kg m^{-3}, respectively, with the kinematic viscosity of the flow $\upsilon = 1.004 \times 10^{-6}$ m^2 s^{-1}. The particle relaxation time is $\tau_p = \rho_p d_p^2/18\rho U$, and the nondimensional particle response time is defined as the particle Stokes number $St = \tau_p u_\tau^2/v$, where the u_τ is the shear velocity [defined as $u_\tau = (\tau_w/\rho)^{1/2}$, where τ_w is the wall shear stress]. Six particle diameters were considered, namely $d_p = 5$, 10, 50, 100, 500, and 1000 μm, with corresponding particle relaxation times, Stokes numbers, and other relevant parameters given in Table 1.

Results and Discussion

Flow field and particle simulations

For a developing single-phase flow, Figure 2a shows a comparison between the present predictions and axial mean velocity profiles measured along the wall bisector ($y/h = 0.5$) in the transverse direction at five downstream stations. The predictions are compared with the data of Gessner et al.[10] and Gessner and Emery[28] obtained at $Re_b = 250{,}000$. It should be noted that the difference between the data

Table 1. Parameters Relevant to the Simulations of Particle Dispersion

d_p (μm)	d_p^+	$St(\tau_p^+)$	τ_p (s)
5	1.32	0.24	3.46×10^{-6}
10	2.64	0.97	1.38×10^{-5}
50	13.19	24.15	3.46×10^{-4}
100	26.37	96.61	1.38×10^{-3}
500	131.87	2415.33	3.46×10^{-2}
1000	263.75	9661.31	1.38×10^{-1}

shown is an indication of experimental scatter since both data sets were obtained using the same experimental apparatus and under similar conditions. It can be seen that the predicted distributions are in good agreement with their experimental counterparts, particularly when the data of Gessner and Emery[28] are used for comparison.

Figure 2b again shows the streamwise development of the axial mean velocity, but now with downstream distance at eight distances from the wall over the interval $0.01 \leq x/h \leq 0.5$ along the wall bisector. It can be seen that the LES performs reasonably well in comparison with the measurements, with the results indicating that velocities in the central region of the flow first increase with downstream distance, reach local peaks, and subsequently decrease to asymptotic values. This peak in the central region is not a secondary flow effect, but the result of shear layer interaction which occur as the boundary layers on opposite walls of the duct merge. The peak in the centerline velocity itself occurs downstream of the location where this first occurs, at $z/h = 32$, indicating that further adjustment of the flow takes place after the initial core flow ceases to exist leading to a nonequilibrium condition at this location.[28] In contrast, velocities near the wall decrease rapidly to their asymptotic values because of the presence of the wall.

Predicted contours of the mean streamwise velocity and secondary flow velocity vectors in the cross-section of the duct are shown in Figure 2c. A high degree of symmetry can be seen around the corner bisector, and the flow vectors reveal the existence of two counter-rotating vortices in the corner of the duct, with four pairs of such vortices in the duct as a whole. The predominant effect of this secondary motion is the induced transport of streamwise momentum toward the corner region from the core of the duct, with isolevels of mean streamwise velocity close to the walls become slightly distorted as a consequence. The maximum value of the secondary velocity in the current simulation is ~2.4% of the bulk velocity, which compares with a value of 2.2% obtained experimentally by Brundrett and Baines.[8]

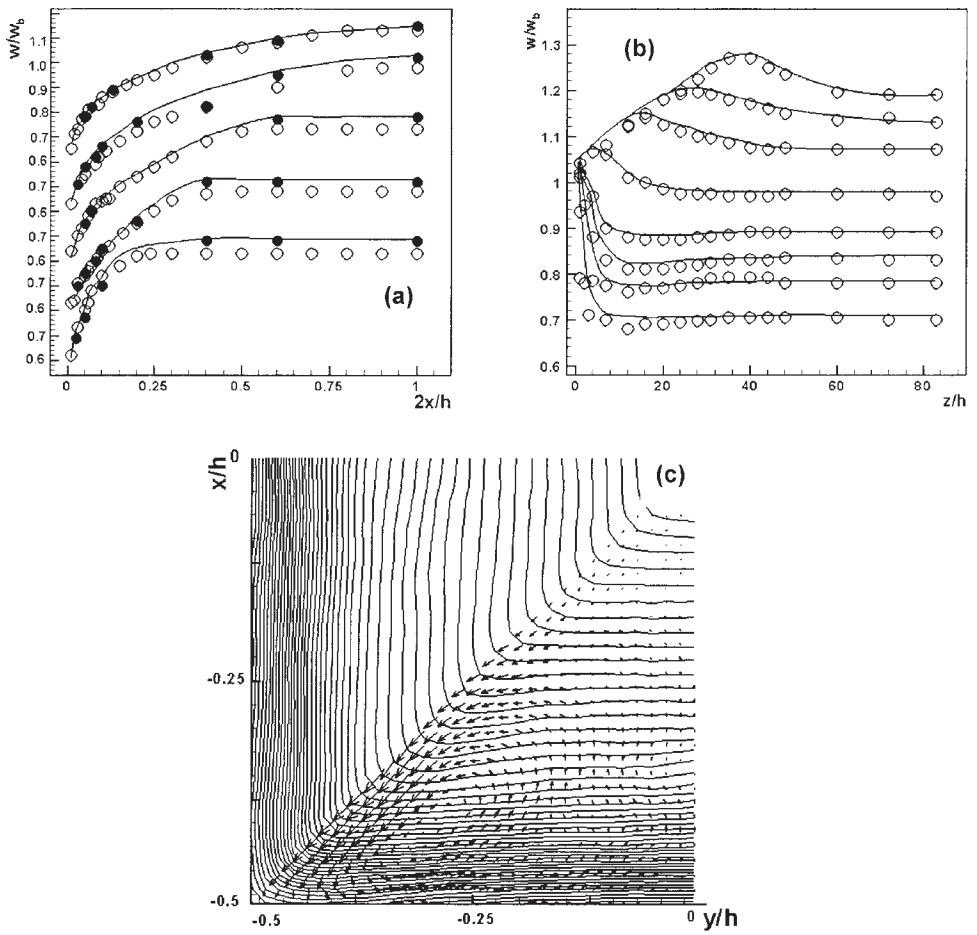

Figure 2. Comparison of predictions with data for streamwise mean velocity along lower wall bisector.

(a) $2z/h = 8$, 16, 24, 40, and 84 (bottom to top); (b) $x/h = 0.01$, 0.02, 0.03, 0.05, 0.1, 0.2, 0.3, and 0.5 (bottom to top); and (c) predicted mean secondary motions on cross-stream plane with mean streamwise velocity contours superimposed (○, Ref. 10; ●, Ref. 28; —, LES).

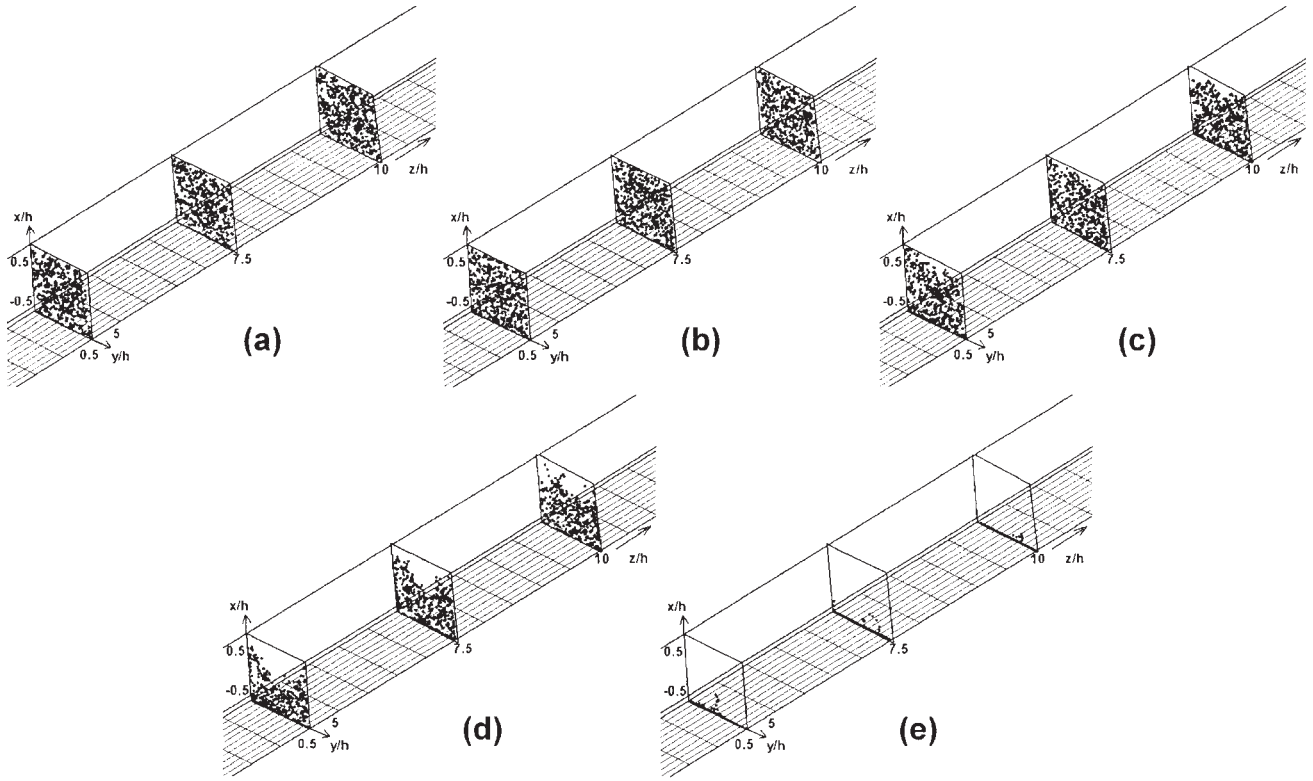

Figure 3. Instantaneous distribution of particles on (*x*, *y*) planes perpendicular to the streamwise direction.

(a) 5 μm ($t^+ = 37{,}211$); (b) 10 μm ($t^+ = 153{,}494$); (c) 50 μm ($t^+ = 153{,}494$); (d) 100 μm ($t^+ = 106{,}981$); (e) 500 μm ($t^+ = 37{,}211$).

Results obtained when particles are introduced to the flow are shown in Figure 3, which gives a perspective view of instantaneous distributions of particles crossing (x, y) planes at various downstream locations. For clarity of presentation, only a fraction of the dispersing particles is plotted. Small particles (5 and 10 μm, Figures 3a,b) are seen to be fully distributed across all cross sections. For medium-size particles (50 and 100 μm, Figures 3c,d), the effect of gravity leads to a progressive accumulation of particles within the lower half of the duct. At larger particle sizes (500 μm and above, Figure 3e), however, within a short time ($t^+ = 37{,}211$), the majority of particles are seen to deposit on the duct floor. In terms of the distribution of particles, the existence of competing gravitational and secondary flow influences clearly lead to different dispersion characteristics depending on particle size, with gravity decoupling particle behavior from the effects of the secondary flow structure which subsequently affects the particle wall-normal distribution and deposition rate, particularly for larger particles.

Particle dispersion statistics

Figures 4a–f show the relationship between the instantaneous particle location in the transverse direction, for all particle sizes, and the distribution of velocity in this direction at $t^+ = 13{,}954$. Location results are plotted in relation to the center-line of the duct, with positive velocities indicating upward movement and negative downward movement. Small particles (5 and 10 μm, Figures 4a,b) are well-dispersed, with gravity having little effect on their distribution, whereas particle velocities are distributed equally in both directions. Medium size particles (50 and 100 μm, Figures 4c,d) are again well dispersed, although most of them (51 and 55%, respectively) tend to be associated with negative velocities acting in the same direction as gravity. For the largest particle sizes (500 and 1000 μm, Figures 4e,f), the majority of particles (84 and 89%, respectively) are approaching the floor of the duct (at $x^+ = -5275$), with their velocities also being mainly directed vertically downwards. Gravity, therefore, has a significant effect on the behavior of these particles.

Figures 4g–i again show the instantaneous distribution of particle position for the larger particles, but at the later time of $t^+ = 200{,}000$. When compared with the results of Figures 4d–f, the particles' velocity distribution is narrower and approximately symmetric about zero. In Figures 4e,f, more particles (75% and 68%, respectively) possess a velocity that is directed toward the duct floor, whereas at the later time (Figures 4h,i), the particle velocity distribution is more symmetrical about $u_p^+ = 0$ with 39% and 42%, respectively, having negative velocities. Physically, at the later time, the particle velocity is much smaller than earlier in the simulations, with the particles being in closer proximity to the floor of the duct. For particles larger than 100 μm, therefore, by $t^+ = 200{,}000$ gravity has caused them to approach and impact on the floor of the duct and to rebound off the wall with a velocity in the opposite direction. After rebounding, however, the particles cannot overcome the effects of gravity

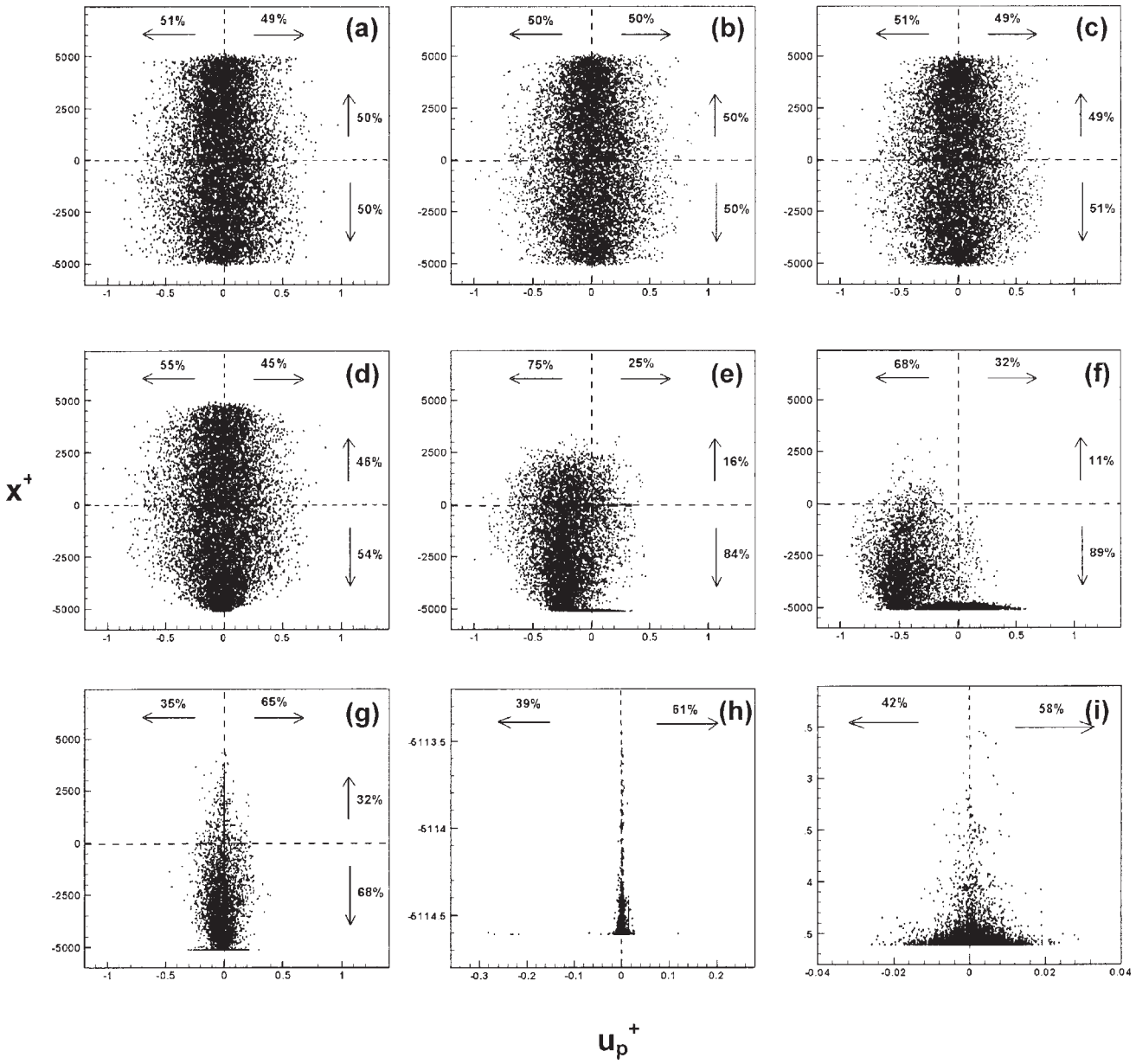

Figure 4. Instantaneous distribution of particle x^+ and u_p^+.

(a) 5 μm; (b) 10 μm; (c) 50 μm; (d) 100 μm; (e) 500 μm; (f) 1000 μm ($t^+ = 13{,}954$); and (g) 100 μm; (h) 500 μm; (i) 1000 μm ($t^+ = 200{,}000$).

and again approach the duct floor. This process then repeats until the particles fully settle down on the lower surface of the duct.

From the results of Figure 4, it is apparent that large (100–1000 μm) particles approach the duct floor with time, whereas smaller (5–50 μm) particles disperse well in the transverse direction, and independently of time. Secondary flow effects may contribute in assisting the smaller particles to overcome the effects of gravity, and the mechanism by which this occurs will be analyzed in later sections.

Turning to results for the spanwise direction, Figures 5a–f show the instantaneous distribution of particle position and velocity in the horizontal direction, again at $t^+ = 13{,}954$, using the same approach as in the previous figure. As gravity has no effect in the direction considered, the influence of the secondary flow dominates particle location. All particle sizes are seen to be evenly dispersed along the spanwise direction, with particle velocities approximately symmetrical about $v^+ = 0$. In addition, velocities in the horizontal direction are found to be of the same order of magnitude as those in the vertical direction (Figures 4a–f).

Figures 5g–i show the instantaneous distribution of the larger particles (100–1000 μm) and their corresponding velocities in the spanwise direction at the later time of $t^+ = 200{,}000$. The particle velocity in the horizontal direction is again approximately symmetrical about $v^+ = 0$ although, when compared with the results of Figures 5d–f, the particles' velocity distribution is narrower, particularly for the

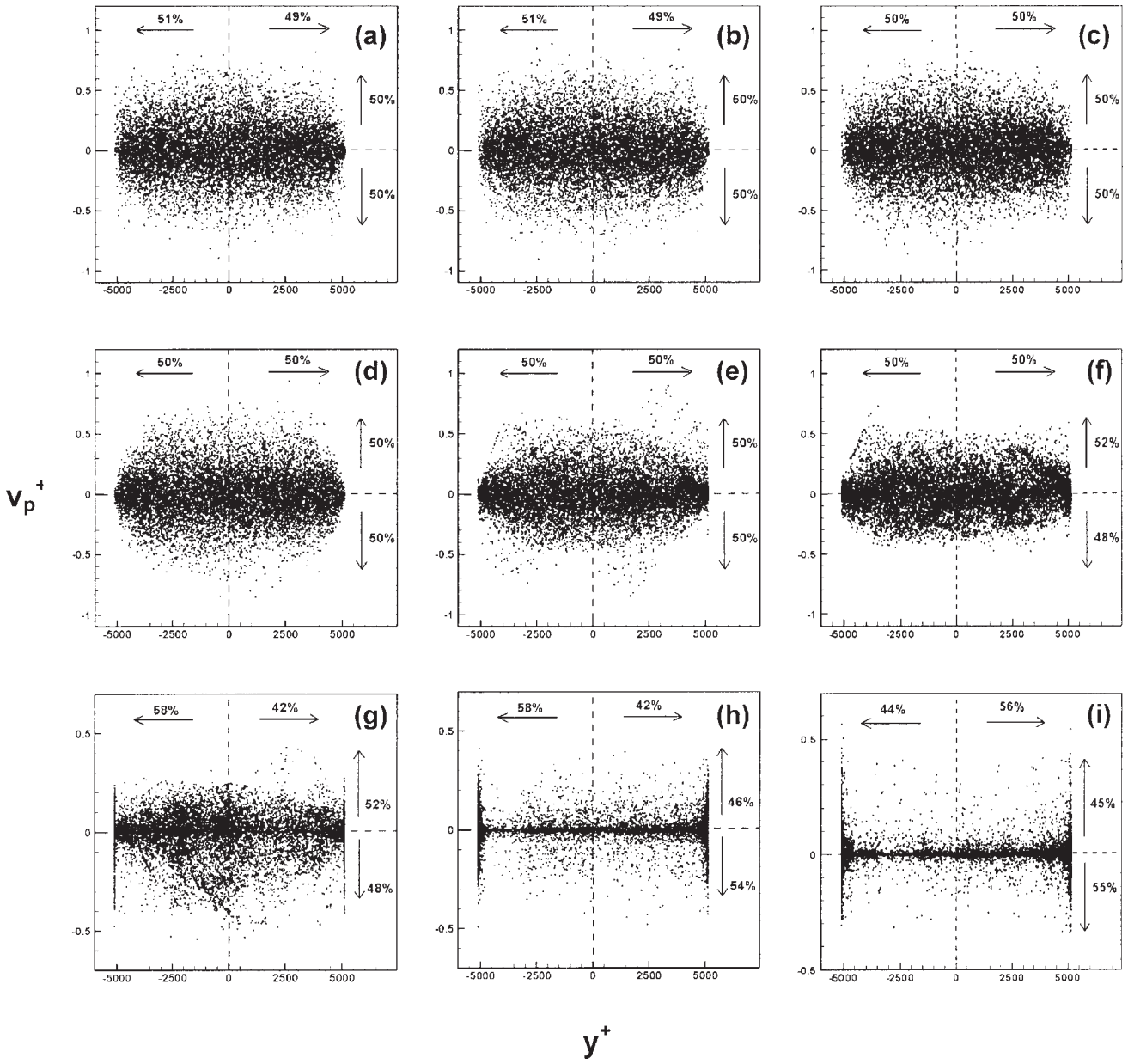

Figure 5. Instantaneous distribution of particle y^+ and v_p^+.

(a) 5 μm; (b) 10 μm; (c) 50 μm; (d) 100 μm; (e) 500 μm; (f) 1000 μm ($t^+ = 13{,}954$); and (g) 100 μm; (h) 500 μm; (i) 1000 μm ($t^+ = 200{,}000$).

largest 500 and 1000 μm particles, as was also found for velocities in the transverse direction. This may contribute to the dominant influence of gravity with time on the motion of the largest particles. It may also be noted that for particles >100 μm, the velocities in the spanwise direction (Figures 5g–i) are larger than those in the transverse direction (Figures 4g–i), with this trend becoming more significant with increasing particle size. This occurs because, at $t^+ = 200{,}000$, the large particles are in close proximity to the floor of the duct where transverse velocities are small but spanwise velocities are relatively large due to the presence of the secondary flow.

Figure 6 gives a detail of predictions derived for the 1000-μm particles at $t^+ = 37{,}211$, in which it is evident that particles on the floor of the duct are prone to accumulate in its corners. This is also evident in the results of Figures 5g–i. This phenomenon can be explained by the presence of the secondary flow. This flow therefore sinks from the center to the corner of the duct, and then moves along the floor turning vertically again toward the duct center. Smaller particles tend to follow this flow pattern which leads to an even distribution in the transverse and spanwise directions. For large particles, however, their size and the greater influence of gravity are not able to follow the flow fully under the influence of the secondary motions. Under their influence, and that of gravity, large particles therefore rapidly sink to the duct corners, but are subsequently unable to flow horizontally and be resuspended from the floor and move toward the duct center.

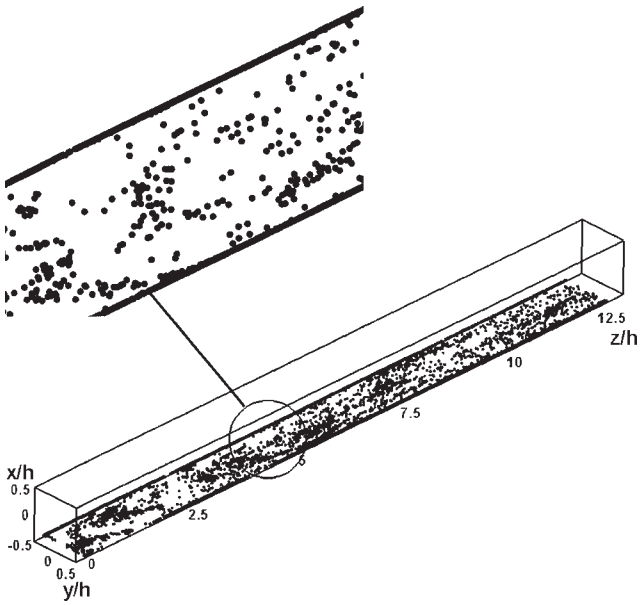

Figure 6. Accumulation of 1000 μm particles at the corners of the duct floor ($t^+ = 37{,}211$).

From the above analysis, it can be concluded that both gravity and secondary flow effects are influential in determining the particle behavior in a square duct flow. For small particles, it is the secondary flow that plays the major role in determining their distribution. For large particles, it is gravity that dominates particle behavior and deposition, although the secondary flow causes particle accumulation at the duct corners.

Particle dispersion function

To study particle dispersion in the duct flow quantitatively, the dispersion function in the transverse, x, direction for particles distributed in the duct can be introduced as follows:

$$D^+_{x(t)} = \left(\sum_{i=1}^{n_t} \frac{\left(x^+_{i(t)} - x^+_{m(t)} \right)^2}{n_t} \right)^{\frac{1}{2}}, \tag{2}$$

where n_t is the total number of particles in the computational domain at time t, $x^+_{i(t)}$ is the particle displacement in the normal direction, and $x^+_{m(t)}$ is the mean value, both relative to the center-line of the duct. Similarly, the dispersion function in the spanwise direction can be obtained from:

$$D^+_{y(t)} = \left(\sum_{i=1}^{n_t} \frac{\left(y^+_{i(t)} - y^+_{m(t)} \right)^2}{n_t} \right)^{\frac{1}{2}}, \tag{3}$$

where $y^+_{i(t)}$ is the particle displacement in the spanwise direction and $y^+_{m(t)}$ is the mean value, again relative to the center-line.

Figures 7a,b show results for the time-dependent particle dispersion in the transverse direction. In Figure 7a, the mean value of the particle displacement is seen to generally decrease with time due to gravity effects, with the rate of deposition increasing with particle size. For large particles (500 and 1000 μm), it only takes a short time ($t^+ = 37{,}211$) for them to approach the duct floor, whereas for medium-sized particles (50 and 100 μm), the rate of deposition is slower and linear with time, with that rate increasing with particle size. For small particles (5 and 10 μm, also shown in detail in the inset of Figure 7a), the mean value of the particle displacement in the transverse direction generally stays constant, although slightly oscillatory. The particle dispersion function (D^+_x) is presented in Figure 7b. It is clear from these results that for particles of 100 μm and larger, the function decreases relatively rapidly with time, whereas for particles up to 50 μm in diameter, the dispersion function remains approximately constant. Closer examination of results for the latter particles does, however, indicate that the 5- and 10-μm particles disperse more in the transverse direction; dispersion for the 50-μm particles increases with time until $t^+ = 106{,}981$, after which point it starts to decrease due to deposition. In close proximity to the duct floor, low-velocity streaks within the flow then cause the larger particles to segregate and concentrate,[29] thereby further affecting particle dispersion. This phenomenon is analyzed in the following section.

Figures 7c,d show equivalent results in the spanwise direction. Mean values of the particle displacement vary with time for all particle sizes, although the variation increases with size indicating that small particles tend to disperse well in the spanwise direction. For particles of 50 μm and larger, the mean value of particle displacement in the transverse direction (Figure 7a) varies from $-5200 < x^+_m < 100$, which is compared with $-800 < y^+_m < 450$ in the spanwise direction (Figure 7c). This suggests that for these particles, the effect of gravity is more significant than that of the secondary flow. However, for small particles (5 and 10 μm), the dispersion in both directions is approximately the same ($-140 < x^+_m < 80$), indicating that gravity effects are unimportant for such particles. Figure 7d shows the dispersion function where for particles of 50 μm and above values generally increase with time and particle size, whereas for 5- and 10-μm particles, this function is approximately constant and only increases slowly with time. This occurs since, under the influence of the secondary flows, larger particles tend to concentrate at the corners of the duct, whereas small particles remain well dispersed.

Particle dispersion in the wall region

Particles deposited in the wall region usually do not attain a uniform distribution in the spanwise direction. In channel flows, previous work[29–32] has reported that particle locations tend to correlate with instantaneous regions of low values of the streamwise velocity, with particles congregating in low-velocity streaks within the flow and avoiding high-velocity regions. In the duct flow, a similar particle behavior can be observed in the results of Figure 8, where the instantaneous distribution of particles in the region $x^+ < 30$ from the duct floor is shown superimposed onto contours of the streamwise fluctuating velocity w' on a (x^+, y^+) plane close to the wall. Small particles (5 and 10 μm) tend to be uniformly distributed in this region, either within low- or high-velocity streaks. However, medium-sized particles (50 and 100 μm)

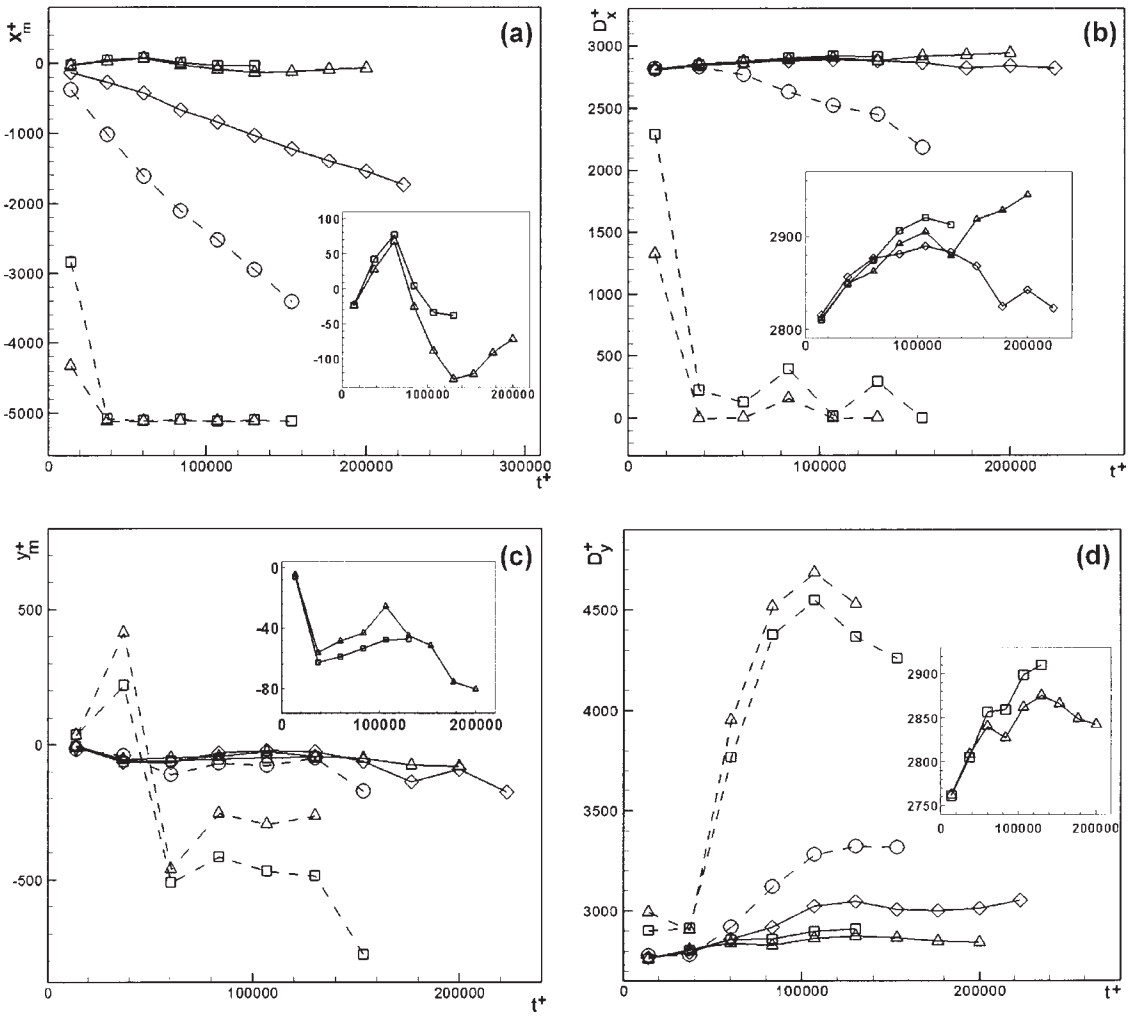

Figure 7. Particle dispersion with time.

(a) Mean displacement and (b) dispersion function in the transverse direction; (c) mean displacement and (d) dispersion function in the spanwise direction (–□–, 5 μm; –△–, 10 μm; –◇–, 50 μm; –○–, 100 μm; -□-, 500 μm; -Δ-, 1000 μm).

segregate into the low-velocity streaks, and this trend continues as particle size increases. The difference between the present duct flow and channel flows[29–32] is that the medium-sized particles tend to concentrate in such regions more than the larger particles, primarily due to the latter concentrating in the corners of the duct.

To give a quantitative measure of the preferential distribution of particles in the low-velocity streaks, a statistical method is used as follows: (i) the area near the duct wall is subdivided into three regions ($0 < x^+ < 30$, $0 < x^+ < 20$, and $0 < x^+ < 10$), with each region also equally divided into 10 slabs, and the average streamwise velocity ($\overline{w_{\text{slab}}}(x)$) of the fluid calculated for each slab; (ii) the number of particles distributed in each slab is determined; (iii) the local streamwise fluctuating velocity of the fluid at the position of the particle is computed according to $w'(x,y,z) = w(x,y,z) - \overline{w_{\text{slab}}}(x)$; and (iv) the number of particles associated with each value of $w'(x, y, z)$ is counted and then normalized by the total number of particles located in the region. The correlation between the particle number density distribution and the fluctuating streamwise velocity in the wall regions is shown in Table 2. These results demonstrate that particles do indeed concentrate in the low-velocity regions, with the particle number density within these regions increasing with particle size due to gravity effects. Comparing particle distribution in regions with negative and positive w' values, for small particle sizes the distribution is relatively uniform, whereas for particles of 50 μm and above, the distribution demonstrates a higher concentration associated with negative w' values (i.e., at velocities lower than the mean). This phenomenon can be explained as follows. For small particles, turbulent vortices are likely to be sufficiently energetic for such particles to be entrained within them, preventing their segregation in low-velocity areas. In contrast, it is more difficult for the vortices to entrain large particles, and hence they tend to be pushed out of the vortices to segregate in low-velocity regions. Hence, particle segregation in the duct flow depends on the particle size or particle response time relative to the local turbulence time scales. These results are largely in line with those obtained for channel flows,[29–32] although the tendency of particles to concentrate in regions associated with negative w' values is lower in the duct than

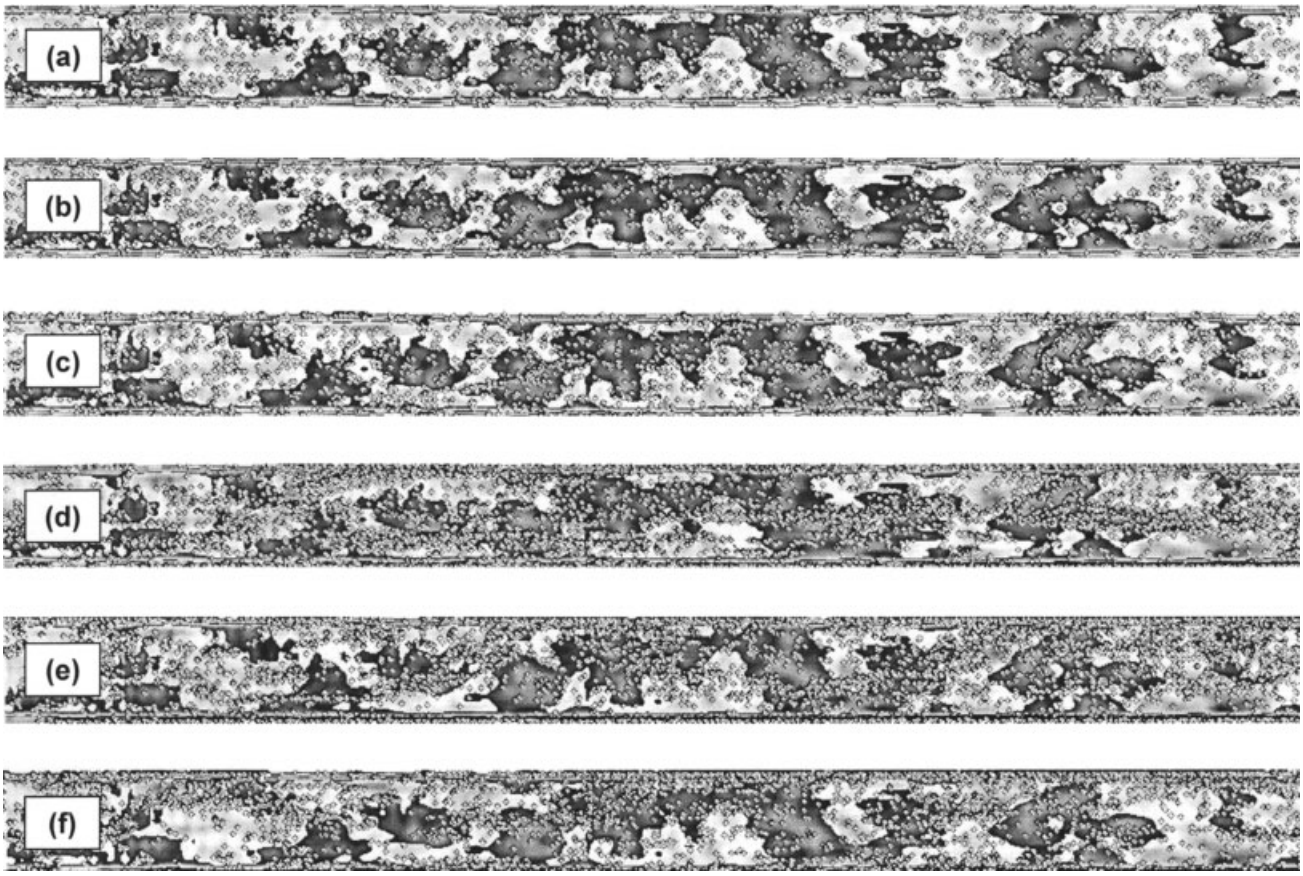

Figure 8. Particle distribution in the wall region on a horizontal plane at $x^+ < 30$ from the duct floor.

Contours are of the streamwise fluctuating velocity w' (dark for $w' < 0$, light for $w' > 0$): (a) 5 μm; (b) 10 μm; (c) 50 μm; (d) 100 μm; (e) 500 μm; and (f) 1000 μm.

in channel flows, which is likely to be caused by the presence of secondary flow effects in the former case.

Particle dispersion mechanisms

Dynamic analysis was used to determine the main forces acting on the particles, i.e., the gravity, drag, and buoyancy forces, with the results given in Table 3. In this table, the drag force was calculated[26] for all three coordinate directions. For particles between 5 and 50 μm, the drag force in the three directions is larger than the gravity force by at least one order of magnitude, indicating that the motion of these particles is dominated by the drag force, not only in the streamwise direction but also in the spanwise and transverse directions. This explains why these particles are well dispersed within the flow, as previously discussed. For 100-μm particles, the drag force in the transverse direction is slightly lower than the gravity force, explaining why particle deposition occurs. For the largest particles, the drag force in the transverse and spanwise directions is significantly lower than the gravity force, indicating that the motion of these particles is dominated by gravity. Therefore, from dynamic analysis, it is clear that the drag force dominates small particle motion in the square duct flow, whereas gravity dominates large particle deposition. In all cases, the buoyancy force is seen to be at least one order of magnitude less than all other forces.

To cast further light on the mechanism of particle dispersion in the duct flow, the relative slip velocity, defined as the difference between the particle and local fluid velocity, may be considered. Figure 9 shows the relative velocity for three different particle sizes. For 5-μm particles, this velocity is small (with

Table 2. Correlation between Particle Number Density Distribution and Fluctuating Streamwise Velocity w' in the Wall Region ($t^+ = 297{,}686$)

	w'/w ($x^+ < 30$-wall)				w'/w ($x^+ < 20$-wall)				w'/w ($x^+ < 10$-wall)			
Particle Size (μm)	$-1<$	$-1\sim0$	$0\sim1$	>1	$-1<$	$-1\sim0$	$0\sim1$	>1	$-1<$	$-1\sim0$	$0\sim1$	>1
5	0	7%	6%	0	0	4%	3%	0	0	1%	1%	0
10	0	8	6	0	0	3	3	0	0	1	1	0
50	0	19	15	0	0	15	11	0	0	12	9	0
100	0	45	39	0	0	42	39	0	0	42	34	0
500	0	54	46	0	0	54	46	0	0	52	47	0
1000	0	56	44	0	0	56	44	0	0	58	42	0

Table 3. Comparison of Effect of Main Forces (Gravity, Buoyancy, and Drag) on Particles ($t^+ = 297{,}686$)

Particle Size (μm)	Gravity (N)	Buoyancy (N)	Drag (N)		
			Transverse	Spanwise	Streamwise
5	1.60×10^{-12}	6.41×10^{-13}	5.70×10^{-11}	5.49×10^{-11}	2.94×10^{-10}
10	1.28×10^{-11}	5.13×10^{-12}	2.22×10^{-9}	2.38×10^{-9}	3.37×10^{-9}
50	1.60×10^{-9}	6.41×10^{-10}	1.27×10^{-8}	1.23×10^{-8}	2.38×10^{-8}
100	1.28×10^{-8}	5.13×10^{-9}	7.91×10^{-9}	3.15×10^{-8}	5.93×10^{-8}
500	1.60×10^{-6}	6.41×10^{-7}	1.47×10^{-8}	4.00×10^{-8}	1.43×10^{-6}
1000	1.28×10^{-5}	5.13×10^{-6}	4.35×10^{-8}	3.06×10^{-8}	4.50×10^{-6}

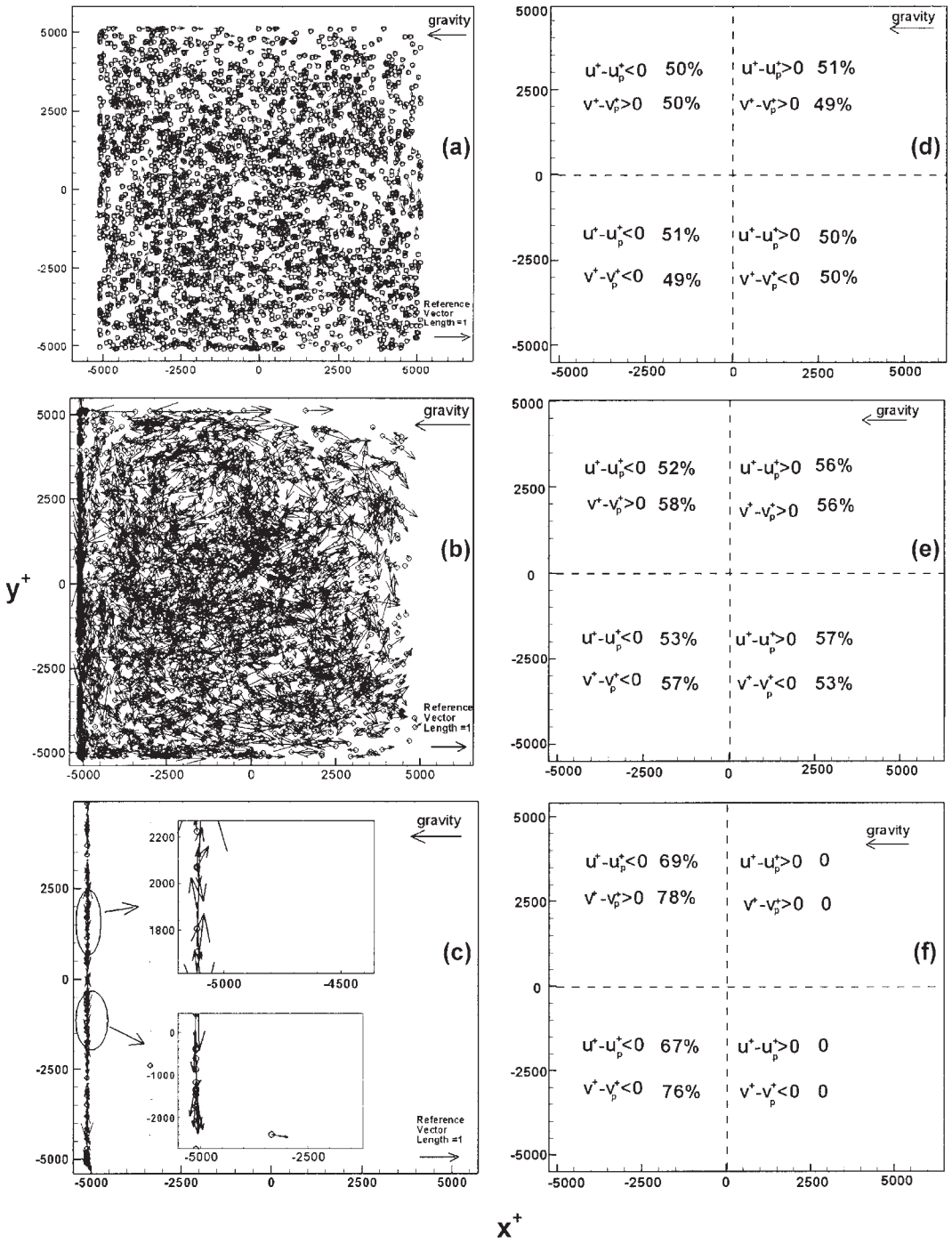

Figure 9. Distribution of relative slip velocity for different particles.

Velocity vectors for (a) 5 μm, (b) 50 μm, and (c) 500 μm; and corresponding percentage of distribution for (d) 5 μm, (e) 50 μm, and (f) 500 μm ($t^+ = 297{,}686$).

Table 4. Mean Relative Slip Velocity between Particle and Fluid ($t^+ = 297{,}686$)

Particle Size (μm)	Mean Relative Slip Velocity		
	$\overline{\lvert u^+ - u_p^+ \rvert}$	$\overline{\lvert v^+ - v_p^+ \rvert}$	$\overline{\lvert w^+ - w_p^+ \rvert}$
5	4.53×10^{-3}	4.38×10^{-3}	2.32×10^{-2}
10	9.92×10^{-3}	2.40×10^{-2}	1.07×10^{-1}
50	1.29×10^{-2}	8.50×10^{-2}	1.53×10^{-1}
100	2.82×10^{-2}	9.00×10^{-2}	1.67×10^{-1}
500	8.42×10^{-2}	9.77×10^{-2}	3.64×10^{-1}
1000	8.73×10^{-2}	3.03×10^{-1}	3.90×10^{-1}

the mean value listed in Table 4), indicating that these particles can follow the fluid motions and disperse well within the duct. For 50-μm particles, because of their larger inertial effects, the magnitude of the relative slip velocity is obviously greater than the smaller particle size (Figure 9 and Table 4), which means that such particles respond slowly to the fluid motion. Lastly, for 500-μm particles, at $t^+ = 297{,}686$, all the particles are approaching the duct floor and the magnitude of the relative slip velocity is larger than for the other particle sizes. In Figure 9c, the insets show that for these particles the relative slip velocity is generally directed toward the duct side walls (at $y^+ = \pm 5275$). Close to the floor of the duct, therefore, the drag force pushes these particles toward the side walls, leading them to accumulate at the corners of the duct. This phenomenon can be attributed to the secondary flow effect, as analyzed previously. Carried by the flow from the center toward the duct corners, large particles tend to have a velocity component directed toward the corner. Because of their significant inertia, these particles will retain this velocity component as they approach the duct floor, where the secondary flow is directed in the opposite direction. The particles then accumulate at the corners of the duct as a consequence.

To quantitatively analyze the secondary flow effect on particle dispersion, the distribution of the relative slip velocity in the four quadrants of the duct is shown in Figures 9d–f. For 5-μm particles, the secondary flow effect on particle dispersion is isotropic due to equal percentage distributions in the four quadrants, indicating that particles closely follow the flow. For 50-μm particles, the distribution of the relative velocity tends to have a high percentage in the secondary flow direction in each of the four quadrants. For example, in the $x^+ < 0$, $y^+ > 0$ quadrant, the secondary flow is in the direction of $u^+ < 0$, $v^+ > 0$, and the distribution of the relative slip velocity of the particles ($u^+ - u_p^+ < 0$, $v^+ - v_p^+ > 0$) has a slightly higher percentage (52% and 58%, respectively) in these directions. This means that the secondary flow will generate a drag force which causes particle dispersion in this direction. For the 500-μm case, at $t^+ = 297{,}686$, all the particles are located below $x^+ = 0$, and the distribution of the relative velocity has a high percentage in the secondary flow direction in the two lower quadrants. This suggests that the relative velocity between the particle and the local fluid will be more directed by the secondary flow. For example, in the $x^+ < 0$, $y^+ > 0$ quadrant, the secondary flow direction is again $u^+ < 0$, $v^+ > 0$, and the distribution of the relative slip velocity of the particles ($u^+ - u_p^+ < 0$, $v^+ - v_p^+ > 0$) has a higher percentage (69% and 78%, respectively) in these directions. Overall, therefore, it can be concluded that the secondary flow in the square duct does affect particle dispersion. For small particles, this flow leads to a uniform particle relative slip velocity distribution in the duct cross section. For large particles, this distribution tends to be most significant in the direction of the secondary flow.

Conclusions

In the square duct flow, competing gravitational and secondary flow effects dictate the dispersion of inertial particles. Gravity decouples particle behavior from the secondary flow structure, thereby affecting the wall-normal distribution and deposition rate of large particles. The secondary flow dominates small particle behavior, causing such particles to be well distributed throughout the flow. Gravity dominates large particle deposition in the transverse direction, although in the spanwise direction, it is the secondary flow that has a significant effect and causes particle concentration in the duct corners.

Analysis of the particle dispersion function shows that in the transverse direction, small particles disperse more with time, whereas medium-sized particles initially disperse until they start to approach to the duct floor when dispersion decreases, with low-velocity regions close to the floor causing particle segregation and concentration. Large particles disperse less with time due to the effects of gravity. Comparing particle dispersion in the spanwise and transverse directions, the gravity effect is found to have a significant influence on the behavior of large particles while having little effect on small particles. Close to the floor of the duct, the particle number density distribution increases with particle size, with a high concentration of large particles associated with flow velocities lower than the mean, while small particles distribute evenly throughout the flow.

From dynamical analysis, the drag force is found to dominate small particle motion, while gravity dominates that of large particles. Relative slip velocities between the particles and the local flow increase with particle size, with values for small particles being relatively low suggesting that they follow the duct flow, whereas for large particles, the slip velocity is high showing that they respond slowly to the fluid motion. In particular, as large particles approach the duct floor, the relative velocity is found to be directed toward the side walls of the duct resulting in a high drag force that concentrates them in the duct corners. From an analysis of the secondary flow effect, it is found that these flows lead small particles to have a uniform relative velocity distribution in the duct cross section, whereas for large particles, the distribution is most significant in the direction of the secondary flow.

Acknowledgements

This work was carried out as part of the TSEC program KNOO, and the authors are grateful to the EPSRC for funding under grant EP/C549465/1. They also express their gratitude to Prof. W. P. Jones for providing the BOFFIN LES code and for many helpful discussions on its use.

Notation

C_D = Stokes coefficient, dimensionless
d_p = particle diameter, m
$D^+_{x(t)}$ = particle dispersion function in transverse direction in wall units, dimensionless
$D^+_{y(t)}$ = particle dispersion function in spanwise direction in wall units, dimensionless
g = gravity, N kg^{-1}
h = width of square duct, m
L_x^+, L_y^+, L_z^+ = duct length in (x^+, y^+, z^+) direction, dimensionless

n_t = total number of particles in computational domain at time t, dimensionless
Re_b = Reynolds number based on flow bulk velocity, dimensionless
Re_p = particle Reynolds number, dimensionless
Re_τ = Reynolds number based on flow friction velocity, dimensionless
St = particle Stokes number, dimensionless
t = time, s
t^+ = time in wall units, dimensionless
Δt = integration time step, dimensionless
Δt^+ = integration time step in wall units, dimensionless
u, v, w = velocity components in (x, y, z) directions, m s^{-1}
u^+, v^+, w^+ = flow velocity components in (x^+, y^+, z^+) directions, dimensionless
u_p^+, v_p^+, w_p^+ = particle velocity components in (x^+, y^+, z^+) directions, dimensionless
u_τ = shear velocity, m s^{-1}
V = fluid velocity (u, v, w), m s^{-1}
V_p = particle velocity, m s^{-1}
$\overline{w_{slab}}\ (x)$ = average streamwise velocity, m s^{-1}
w' = local streamwise fluctuating velocity at particle position, m s^{-1}
w_b = bulk flow velocity in streamwise direction, m s^{-1}
x, y, z = Cartesian coordinate system, m
x^+, y^+, z^+ = Cartesian coordinate system in wall units, dimensionless
$\Delta x^+, \Delta y^+, \Delta z^+$ = grid resolution in (x^+, y^+, z^+) directions, dimensionless
$x_{i(t)}^+$ = particle displacement in transverse direction in wall units, dimensionless
$X_{m(t)}^+$ = mean value of particle displacement in transverse direction in wall units, dimensionless
$y_{i(t)}^+$ = particle displacement in spanwise direction in wall units, dimensionless
$Y_{m(t)}^+$ = mean value of particle displacement in spanwise direction in wall units, dimensionless

Greek letters

ρ = fluid density, kg m^{-3}
ρ_p = particle density, kg m^{-3}
τ_p = particle relaxation time, s
τ_w = wall shear stress, N m^{-2}
ν = kinematic viscosity, m^2 s^{-1}

Literature Cited

1. Tang L, Wen F, Yang Y, Crowe CT, Chung JN, Troutt TR. Self-organizing particle dispersion mechanism in a plane wake. *Phys Fluids A*. 1992;4:2244–2251.
2. Ling W, Chung JN, Troutt TR, Crowe CT. Direct numerical simulation of a three-dimensional temporal mixing layer with particle dispersion. *J Fluid Mech*. 1998;358:61–85.
3. Fan JR, Zheng YQ, Yao J, Cen KF. Direct simulation of particle dispersion in a three-dimensional temporal mixing layer. *Proc R Soc Lond A*. 2001;457:2151–2166.
4. Yuu S, Yasukouchi N, Hirosawa Y, Jotaki T. Particle turbulent diffusion in a dust laden round jet. *AIChE J*. 1978;24:509–519.
5. Fairweather M, Hurn JP. Validation of an anisotropic model of turbulent flows containing dispersed solid particles applied to gas-solid jets. *Comput Chem Eng*. 2007;32:590–599.
6. Morsi SA, Alexander AJ. An investigation of particle trajectories in two-phase systems. *J Fluid Mech*. 1972;55:193–208.
7. Yao J, Ji F, Liu L, Fan JR, Cen KF. Direct numerical simulation on the particle flow in the wake of circular cylinder. *Prog Nat Sci*. 2003;13:379–384.
8. Brundrett E, Baines WD. The production and diffusion of vorticity in duct flow. *J Fluid Mech*. 1964;19:375–394.
9. Launder BE, Ying WM. Secondary flows in ducts of square cross-section. *J Fluid Mech*. 1972;54:289–295.
10. Gessner FB, Po JK, Emery AF. *Measurements of developing turbulent flow in a square duct*. In: Durst F, Launder, Schmidt FW, Whitelaw JH, editors. *Turbulent Shear Flows 1*. New York: Springer-Verlag, 1979:119–136.
11. Gavrilakis S. Numerical simulation of low-Reynolds-number flow through a straight square duct. *J Fluid Mech*. 1992;244:101–129.
12. Madabhushi RK, Vanka SP. Large eddy simulation of turbulence-driven secondary flow in a square duct. *Phys Fluids A*. 1991; 3:2734–2745.
13. Winkler CM, Rani SL, Vanka SP. Preferential concentration of particles in a fully developed turbulent square duct flow. *Int J Multiphase Flow*. 2004;30:27–50.
14. Sharma G, Phares DJ. Turbulent transport of particles in a straight square duct. *Int J Multiphase Flow*. 2006;32:823–837.
15. Robinson SK. Coherent motions in the turbulent boundary layer. *Annu Rev Fluid Mech*. 1991;23:601–639.
16. Germano M. A proposal for redefinition of the turbulent stresses in the filtered Navier-Stokes equations. *Phys Fluids*. 1986;19:2323–2324.
17. Piomelli U, Liu J. Large eddy simulation of rotating channel flows using a localized dynamic model. *Phys Fluids*. 1995;7:839–848.
18. di Mare L, Jones WP. LES of turbulent flow past a swept fence. *Int J Heat Fluid Flow*. 2003;24:606–615.
19. Jones WP. *BOFFIN: A Computer Program for Flow and Combustion in Complex Geometries*. Imperial College of Science, Technology and Medicine, 1991.
20. Rhie CM, Chow WL. Numerical study of the turbulence flow past an airfoil with trailing edge separation. *AIAA J*. 1983;21:525–1532.
21. Choi H, Moin P. Effect of the computational time step on numerical solutions of turbulent flow. *J Comput Phys*. 1994;113:1–4.
22. Fan JR, Yao J, Cen KF. Antierosion in a 90° bend by particle impaction. *AIChE J*. 2002;48:401–1412.
23. Saffman PG. Lift on a small sphere in a slow shear flow. *J Fluid Mech*. 1965;22:385–400.
24. Mclaughlin JB. Aerosol particle deposition in numerically simulated channel flow. *Phys Fluids*. 1989;1:1211–1224.
25. Yao J, Zhang Y, Wang CH, Matsusaka S, Masuda H. Electrostatics of the granular flow in a pneumatic conveying system. *Ind Eng Chem Res*. 2004;43:7181–7199.
26. Yao J, Zhang Y, Wang CH, Liang YC. On the electrostatic equilibrium of granular flow in pneumatic conveying systems. *AIChE J*. 2006;52:3775–3793.
27. Armenio V, Fiorotto V. The importance of the forces acting on particles in turbulent flows. *Phys Fluids*. 2001;13:2437–2440.
28. Gessner FB, Emery AF. The numerical prediction of developing turbulent flow in rectangular ducts. *J Fluid Eng*. 1981;103:445–455.
29. Pan Y, Banerjee S. Numerical simulation of particle interactions with wall turbulence. *Phys Fluids*. 1996;8:2733–2755.
30. Pedinotti S, Mariotti G, Banerjee S. Direct numerical simulation of particle behavior in the wall region of turbulent flows in horizontal channels. *Int J Multiphase Flow*. 1992;18:927–941.
31. Eaton JK, Fessler JR. Preferential concentration of particles by turbulence. *Int J Multiphase Flow*. 1994;20:169–209.
32. Zhang HF, Ahmadi G. Aerosol particle transport and deposition in vertical and horizontal turbulent duct flows. *J Fluid Mech*. 2000; 406:55–80.

Manuscript received May 6, 2008, revision received Oct. 6, 2008, and final revision received Dec. 3, 2008.